9-2005

Time-of-flight Emission Profiles of the Entire Plume Using Fast Imaging During Pulsed Laser Deposition of $YBa_2Cu_3O_{7-x}$

Carl J. Druffner
Air Force Institute of Technology

Glen P. Perram
Air Force Institute of Technology

Rand R. Biggers
Air Force Research Laboratory

Recommended Citation

Carl J. Druffner, Glen P. Perram, Rand R. Biggers; Time-of-flight emission profiles of the entire plume using fast imaging during pulsed laser deposition of YBa2Cu3O7−x . Rev Sci Instrum 1 September 2005; 76 (9): 093101. https://doi.org/10.1063/1.2018503

Review of Scientific Instruments

RESEARCH ARTICLE | AUGUST 23 2005

Time-of-flight emission profiles of the entire plume using fast imaging during pulsed laser deposition of $YBa_2Cu_3O_{7-x}$

Carl J. Druffner; Glen P. Perram; Rand R. Biggers

Rev Sci Instrum 76, 093101 (2005)
https://doi.org/10.1063/1.2018503

AIP Publishing

Time-of-flight emission profiles of the entire plume using fast imaging during pulsed laser deposition of $YBa_2Cu_3O_{7-x}$

Carl J. Druffner and Glen P. Perram[a)]
Department of Engineering Physics, Air Force Institute of Technology, 2950 Hobson Way, Wright-Patterson Air Force Base, Ohio 45433-7765

Rand R. Biggers
Materials and Manufacturing Directorate, Air Force Research Laboratory, 2977 Hobson Way, Wright-Patterson Air Force Base, Ohio 45433-7746

(Received 14 September 2004; accepted 12 July 2005; published online 23 August 2005)

Emission time-of-flight (TOF) profiles have been obtained using gated imagery to further the process control during the pulsed laser deposition of the high temperature superconductor, $YBa_2Cu_3O_{7-x}$. An intensified charge coupled device array was used to obtain a sequence of plume images at 10 ns temporal resolution and 0.2 mm spatial resolution. Plume imagery is transformed to TOF profiles and pulse-to-pulse variations removed using physically based smoothing techniques. Comparison with non-imaging sensors establishes excellent agreement, with systematic uncertainties in streaming speed and temperatures of less than 15% and 8%, respectively. The resulting streaming speeds of $0.4-1.2\times10^6$ cm/s and characteristic temperatures of 20 000–200 000 K are characterized across the full plume. This new imaging TOF technique enables the monitoring of the complete evolution of speed distributions. Indeed, significant deviations from the forward-directed Maxwellian speed distributions are observed. [DOI: 10.1063/1.2018503]

I. INTRODUCTION

Pulsed laser deposition (PLD) has become an important method for the production of oriented, high quality thin films from nanometer to micron thicknesses,[1,2] including the fabrication of 1 m length wires coated with the high temperature superconductor, $YBa_2Cu_3O_{7-x}$ (YBCO).[3–6] There are many control variables that affect the deposition conditions and quality of the deposited films,[7] and *in situ* monitoring techniques are required to extend the process for repeatable manufacturing of the long lengths (~1 km) of high quality, defect free superconducting wires necessary for power generation.[8] Many optical techniques for monitoring the energetic gas phase plume arising from PLD processes have been developed, including time-of-flight (TOF) spectroscopy using mass spectrometers,[9] ion probes,[10] and emission spectroscopy,[7,8] spectrally resolved visible emission[11] and absorption[10] techniques, and fast imagery.[10] Establishing correlations between the plume dynamics and deposited film properties such as critical currents is an important next step in the development of improved PLD feedback sensors.[7,9]

Time-of-flight diagnostics are particularly useful in characterizing the kinetic energy distributions of various plume constituents and can be used as a deposition control parameter.[1,7] The plumes exhibit high kinetic energies (~50 eV) and the oxygen background gas (~200 mTorr) serves to thermalize the plume over distances of 1–20 cm.[10] TOF spectroscopy usually involves monitoring the flux (or concentration) of some specie(s) at a specified distance from the target as a function of time. Mass spectrometry and fast Langmuir probes are typically used to monitor the significant ionic content of the plume.[1] Neutral species are monitored by emission using spectrally filtered photodiodes or photomultiplier tubes (PMTs),[7,8,12] or by laser absorption[13,14] or laser induced fluorescence[14–16] techniques for ground states. Typically, the detector's collection volume provides a spatial resolution of $\geqslant$1 mm. Translating the detector is required to monitor different locations within the plume.

Fast plume imagery using gated intensified charged coupled device (ICCD) arrays have previously been used to characterize the fluid dynamic effects, shock structure, and reactive scattering of PLD plumes.[1,10] In the present work, a noninvasive emission TOF technique is developed based on such fast plume imagery that provides a high-resolution spatial map of the TOF spectra. By comparing the ICCD imaging and scanned PMT emission TOF techniques, an assessment of the effects of spatial resolution on observed kinetic energy distributions is attainted. Issues associated with pulse-to-pulse variations and longer-term temporal drift in PLD TOF measurements are also addressed. Finally, the power of the imaging technique is demonstrated by establishing the dynamics of the kinetic energy distributions. Deviations from the forward-directed Maxwellian distributions typically used to characterize PLD TOF spectra are clearly demonstrated.

II. EXPERIMENT

The pulsed laser deposition apparatus has been described in detail previously.[7,8] A Lambda Physik LPX 305i excimer

[a)]Author to whom correspondence should be addressed; electronic mail: glen.perram@afit.edu

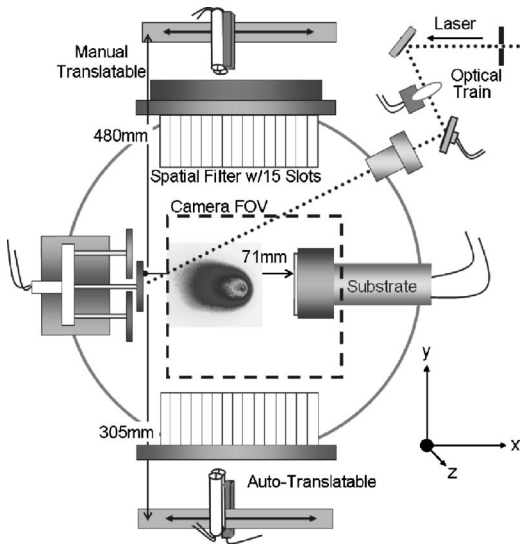

FIG. 1. Pulsed laser deposition chamber with imaging and translatable time-of-flight sensors.

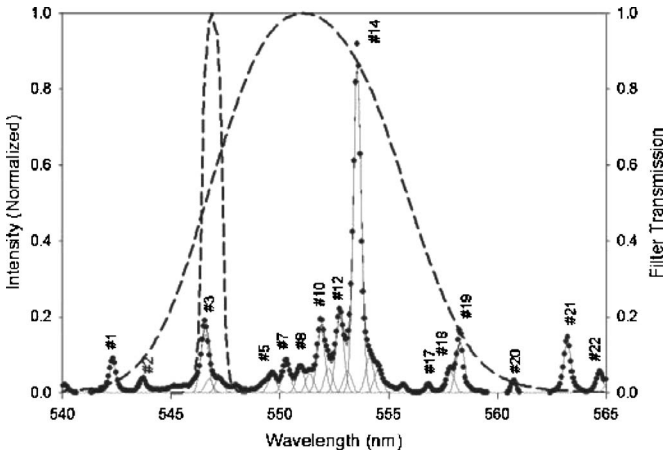

FIG. 2. Time integrated emission spectrum near $\lambda = 550$ nm recorded by a fiber coupled grating spectrometer with large field of view to observed the complete plume.

laser provides a ~350–450 mJ, 17 ns pulse at $\lambda = 248$ nm deposited in a $\Delta x \cong 2.2$ mm by $\Delta y \cong 15$ mm spot ($5.7–8.7 \times 10^7$ W/cm^2 at target) typically at a 4 Hz repetition rate. The laser energy is delivered to a rotating tetragonal-YBCO target at a 45° via an aperture, turning mirror, and two-axis scanning mirror. The 38 cm diam deposition chamber contains a substrate heater assembly (~900 °C), pressure control for 10^{-5}–1 Torr oxygen background gas, 15 cm fused quartz windows on both sides, and a 20 cm Pyrex window on top.

The geometry for both the fast imagery and scanned PMT emission sensors is illustrated in Fig. 1. A Princeton Instruments PI-Max intensified 512×512 CCD array with $f/1.4$ lens was used to image the plume from above ($+z$ direction). The camera was located at 520 mm above the plume centerline, with a field of view of 100×100 mm (0.2 mm/pixel). The view included the substrate heater, but the target is recessed in a port extension tube and is obscured for the first 10 mm from the target. The cross-plume (y) view is sufficient to capture the full plume. The depth of field for the $f/1.4$ lens was about 6 mm. The camera was gated (10 ns) with an ST-133 controller triggered by a photodiode observing the laser pulse. The temporally evolving plume was monitored by increasing the delay between laser trigger and the camera gate after 140–200 laser pulses, in 50–250 ns intervals. A larger temporal sampling of the images could be achieved with a smaller interval between gates, but with a corresponding increase in data acquisition time.

Four Hamamatsu R74004-04 PMTs were also used to monitor the TOF emission from both sides of the chamber and could be translated across 15 slots, which act as spatial filters. The slots are each 4 mm wide by 60 mm long and located in the vacuum chamber just inside the fused quartz windows. The full width of the slot assembly is 72 mm, with the first slot located at 13 mm from the target, and the 13th slot centered at about 2 mm in front of the substrate. Further spatial filtering is provided by placing each PMT in a 90 mm (or 200 mm) long by 15 mm diam cylinder with a 1 mm slit on the chamber end. Two of the PMTs, PMT 1 (top) and PMT 2 (bottom), are located 300 mm from the chamber center line on a computer controlled translation stage. The other two PMTs, PMT 3 (bottom) and PMT 4 (top), are located on the opposing side of the chamber, 458 mm from the center line.

Several band pass filters were employed with both the ICCD camera and PMT sensors to emphasize the emission from various atomic constituents. Two narrow band filters were used to isolate the emission from neutral barium (Ba I $\lambda = 767 \pm 1$ nm) and neutral yttrium (Y I $\lambda = 547 \pm 1$ nm). A third, broader filter was used to observed blended emission from both Y I and Ba I at $\lambda = 550 \pm 5$ nm. A moderate resolution (0.4 nm) spectrum of the plume was recorded to assign all atomic line emission within the filter band pass, as shown for the 550 nm region in Fig. 2. The most intense feature is assigned to the Ba I $^1S_0 \leftarrow {}^1P^0{}_1$ transition, which terminates on the ground state, and thus is significantly affected by radiation trapping.[17] Of the other 23 most intense, relevant atomic lines in this region,[18] only one, the weak Y I $^2F_{5/2} \leftarrow {}^4D^0{}_{7/2}$, is not observed, as demonstrated in Table I. The observed spectrum was fit to the set of 24 atomic lines with a common Gaussian line shape [0.428 nm full width half maximum (FWHM)]. For the broad band filter, the resulting line intensities and 62% peak transmission of the filter yields the fraction of emission due to neutral atomic barium as about 52%, which depends (~5% variance) on the deposition condition. Most of the remaining emission is attributed to Y I (37%) and Y II (8%). In contrast, the Y I $\lambda = 547 \pm 1$ nm filter isolates the emission to Y I and Y II, with 80%–85% of the intensity attributed to neutral yttrium. The Ba I $\lambda = 767 \pm 1$ nm filter provides nearly complete isolation of emission from neutral barium.

III. RESULTS

A. PMT sensor

Typical TOF spectra observed by the PMTs in these YBCO depositions exhibit ablated atom kinetic energies of ~50 eV and energy distributions with widths of ~5–20 eV,

TABLE I. Spectral assignments for Fig. 2 near λ=550 nm.

Peak	Emitter	Assignment	Intensity	% of signal
1	Ba I	$^3P^o_0 \leftarrow {}^3D_1$	2.73±0.21	0.1
2	Y I	$^2F_{7/2} \leftarrow {}^2D_{5/2}$	1.07±0.21	0.2
3	Y I	$^4F_{9/2} \leftarrow {}^4G_{11/2}$	5.46±0.50	4.3
4	Y I	$^2F_{5/2} \leftarrow {}^2F^o_{5/2}$	1.31±0.68	1.1
5	Y II	$^3P_1 \leftarrow {}^3P^o_2$	1.46±0.22	1.5
6	Y II	$^3P_2 \leftarrow {}^3P^o_2$	1.73±0.21	2.7
7	Y I	$^2F_{7/2} \leftarrow {}^2F^o_{7/2}$	2.86±0.21	4.6
8	Y II	$^3F_2 \leftarrow {}^1D^o_2$	2.23±0.28	3.6
9	Y I	$^4P_{5/2} \leftarrow {}^4F^o_{5/2}$	1.77±0.28	2.9
10	Ba I	$^3P^o_1 \leftarrow {}^3D_2$	6.00±0.47	9.6
11	Y I	$^2F_{5/2} \leftarrow {}^2G^o_{7/2}$	2.27±0.46	3.6
12	Y I	$^4F_{7/2} \leftarrow {}^4G^o_{9/2}$	7.33±0.49	11.2
13	Y I	$^2P_{3/2} \leftarrow {}^4P^o_{5/2}$	2.01±0.48	3.0
14	Ba I	$^1S_0 \leftarrow {}^1P^o_1$	29.94±0.29	42.2
15	⋯	⋯	3.47±0.30	4.6
16	Y I	$^2F_{5/2} \leftarrow {}^4D^o_{5/2}$	2.15±0.33	2.6
17	Y I	$^4P_{5/2} \leftarrow {}^2G^o_{7/2}$	0.67±0.21	0.4
18	Y I	$^2F_{3/2} \leftarrow {}^2G^o_{9/2}$	1.97±0.26	0.7
19	Y I	$^4F_{5/2} \leftarrow {}^4G^o_{7/2}$	4.60±0.26	1.2
20	Y I	$^4F_{9/2} \leftarrow {}^4G^o_{9/2}$	0.76±0.21	0.0
21	Y I	$^2F_{7/2} \leftarrow {}^4D^o_{7/2}$	4.68±0.21	0.0
22	Ba I	$^1P^o_1 \leftarrow {}^3D_2$	1.66±0.28	0.0
23	Y I	$^2D^o_{5/2} \leftarrow {}^4D_{7/2}$	1.03±0.28	0.0
24	Ba I	$^1P^o_1 \leftarrow {}^3D_1$	3.33±0.21	0.0

as shown using the broadband λ=550±5 nm filter in Fig. 3. During well controlled depositions, where the peak in the TOF spectra is used as a control parameter,[7,8] the repetitive TOF spectra from an individual PMT exhibit less than 1% deviation in peak time, but typically 8% in width and 6% in amplitude over a collection time of several minutes. This variability is significantly reduced when TOF spectra from multiple laser pulses are averaged. Figure 3 illustrates the TOF spectra for an average of 640 laser shots for three PMTs viewing the same target distance. Note that viewing volume discrepancies can be easily introduced when attempting to aim multiple PMTs at the same chamber position or when trying to relocate a translatable sensor. In Fig. 3, a 17%, variation in TOF width and 2% TOF peak time are observed for two PMT's located on top of one another on one side of the chamber and a third PMT located on the opposite side of the chamber. Clearly, the systematic errors in these TOF spectra are larger than the low statistical uncertainties.

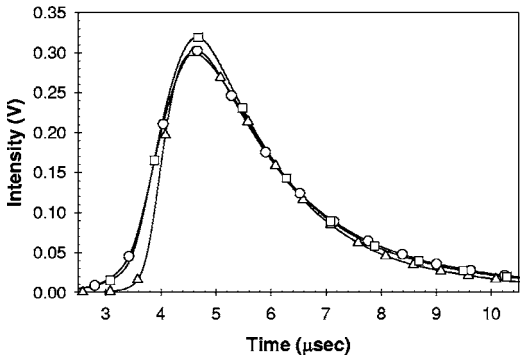

FIG. 3. Averaged time-of-flight profiles recorded using the broad band λ =550±5 nm filter from three PMT sensors: (□) PMT 2, (○) PMT 3, and (△) PMT 4, viewing the same volume at x=3.6 cm for 200 mTorr oxygen. More than 4000 time samples are represented by the solid line. Symbols are added only for identification.

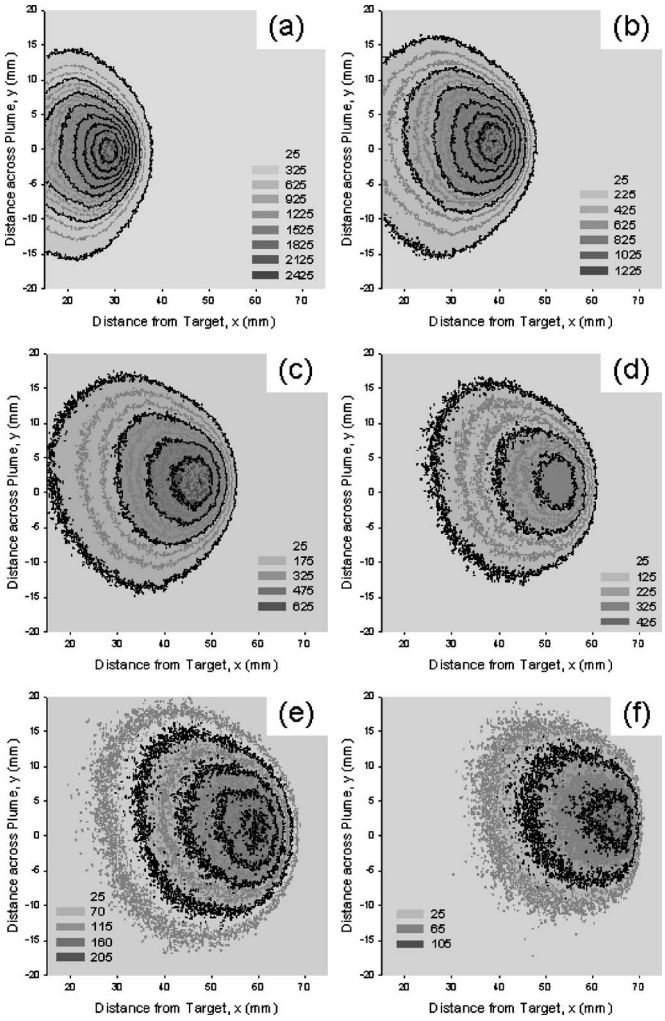

FIG. 4. A sequence of ICCD images at λ=550±5 nm captured at time delays of: (a) 3, (b) 5, (c) 7, (d) 9, (e) 11, and (f) 13 μs after ablation. Grey scale levels indicate ICCD intensity in counts.

B. CCD array imagery

The intensified CCD movies capture a great deal of information, including hydrodynamics,[1] angular distributions of ablated material,[1] and as shown in this work, the emission TOF spectra for all locations within the plume simultaneously. For example, a sequence of several barium filtered images for a 200 mTorr deposition is shown in the contour plots of Fig. 4. The plume emission reaches the substrate at ~12.5 μs with a significant decrease in emission intensity as the plume propagates. The expansion Mach number increases to $M \sim 5$ and the plume is highly forward peaked.

To obtain emission TOF spectra from the imagery, the intensities for all CCD pixels with a constant distance to the target (the row, x=constant) are summed. This summed intensity for multiple image frames provides the temporal evolution necessary to construct the TOF spectrum, as shown in Fig. 5. An extensive series of TOF spectra for 125 different chamber distances of 29–54 mm are obtained with a spatial

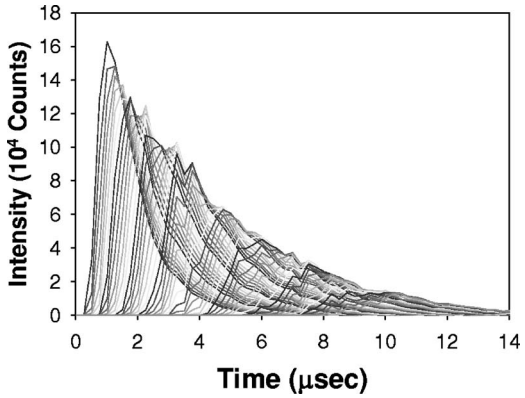

FIG. 5. Time-of-flight profiles from ICCD imagery at $\lambda=550\pm5$ nm for target distances $x=29-54$ mm at 200 mTorr oxygen. There are repeated groups of seven gray shaded lines for a total of 125 target distances in intervals of $\Delta x=0.2$ mm.

resolution of about 0.2 mm. In Fig. 5, only every fifth TOF spectra of the 125 recorded is shown for clarity of illustration. The spectra suffer from both jitter and flicker associated with pulse-to-pulse variation in the plumes. Intensity variations up to 20% (flicker) and variations in the plume center-of-mass (jitter) of up to 3 mm are observed. Two physically based methods for averaging these fluctuations have been developed and the resulting TOF spectra provided in Fig. 6.

The jitter was addressed using a drag model for plume propagation:[1]

$$x = x_f(1 - e^{-k_d t}) + x_0, \tag{1}$$

where x_f=emissive plume stopping position, k_d=drag decay rate, and x_0=target location ($x_0 \approx 0$).

A fit of Eq. (1) to the plume center of mass for the conditions of Fig. 5 provides $x_f=99\pm2$ mm and $k_d=0.064\pm.003$ μs^{-1}. The effects of jitter are largely removed by shifting the plume center of mass for each frame to the average value represented by the curve fit to Eq. (1). We have chosen to characterize the plume position by the center of mass of the intensity distribution, instead of the shock front location, to exploit the entire plume in the jitter averaging. The drag model of Eq. (1) has been previously applied to the total visible emission from YBCO shock fronts for similar PLD conditions, yielding $x_f=30$ mm and $k_d=0.36$ μs^{-1}.[11] The shorter stopping distance and faster decay

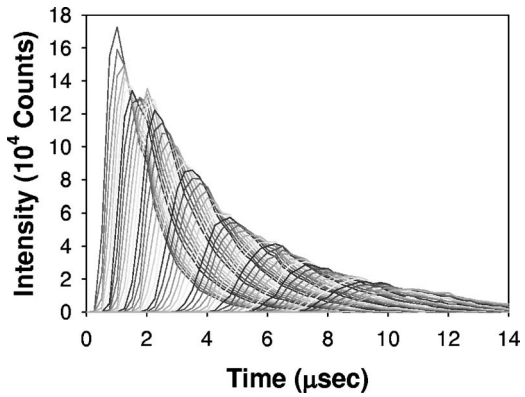

FIG. 6. Time-of-flight profiles corresponding to the data from Fig. 4, adjusted for both jitter and flicker.

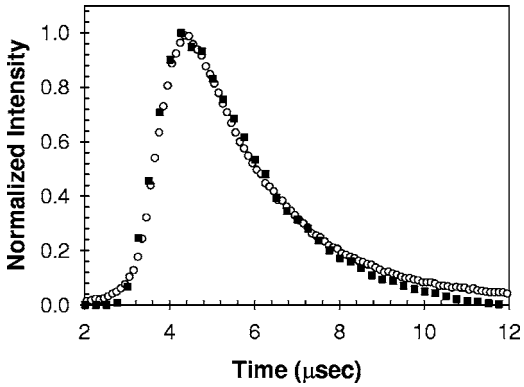

FIG. 7. Comparison of PMT (○) and ICCD (■) time-of-flight profiles at $\lambda=550\pm5$ nm collected on the same deposition at $x=3.6$ cm and 200 mTorr.

may be attributed to less fluence at the target, lower background pressure, and smaller angular divergence due to a larger spot size. Explosive models,[1,19] empirical fits, or data filtering could also be used to reduce the plume jitter.

The plume intensity fluctuations are handled similarly, by evaluating the exponential decay of intensity:

$$I(t) = I_0 e^{-k_2(t-t_0)}, \tag{2}$$

where I_0 is the intensity at $t=t_0$ and k_2 is the intensity decay rate. A fit of spatially average plume intensity to Eq. (2) for the data of Fig. 5, yields a decay rate of $k_2=0.236\pm0.004$ μs^{-1}. Adjusting the observed TOF spectra to the average decaying intensity further reduces the variability in TOF spectra. The result of averaging for both flicker and jitter is shown in Fig. 6.

C. Comparison of PMT and imagery TOF spectra

Figure 7 compares the TOF spectra from the fixed PMT sensor and the ICCD camera at the midpoint in the chamber, $x=38$ mm. The two sensors agree quite well, considering the shot-to-shot variability in the ICCD images and the dependence on viewing volume exhibited for the PMT sensors. Characterization of the TOF profiles in terms of speed distributions is provided in further detail below.

IV. DISCUSSION

Time-of-flight data are often represented by a modified Maxwell–Boltzmann distribution with a forward directed (center-of-mass shifted) streaming speed:[1,12]

$$f(v) = A\left(\frac{m}{2\pi k}\right)^{3/2} v^n e^{-m(v-u)^2/2kT} dv, \tag{3}$$

where m=mass of the emitter, k=Boltzmann constant, v=speed (along propagation direction, x), u=streaming speed, T=stream temperature describing the width of the speed distribution, and n=integer exponent, typically 3–4.

Using the time of arrival, $t=x/v$, the resulting temporal profile is

TABLE II. Speed distributions from PMT sensors located at $x=3.6$ cm from TOF profiles presented in Fig. 3.

	u (10^3 cm/s)			T (1000 K)		
n	PMT 1	PMT 2	PMT 3	PMT 1	PMT 2	PMT 3
0	723.3±0.5	715.7±0.5	719.8±0.6	52.8±0.2	58.0±0.3	42.6±0.3
1	675.7±0.7	662.2±0.7	681.6±0.8	55.8±0.3	61.8±0.3	44.6±0.3
2	622.4±1.0	601.5±1.1	639.8±1.1	59.1±0.3	66.0±0.4	46.8±0.4
3	562.3±1.4	532.0±1.7	593.8±1.5	62.9±0.4	70.9±0.5	49.1±0.4
4	494.3±3.5	452.0±2.4	543.0±2.1	67.2±0.5	76.4±0.6	51.7±0.5
5	416.7±3.5	358.8±4.4	486.6±3.4	72.0±0.7	82.7±0.8	54.6±0.6
6	184.3±7.9	151.2±9.9	179.6±17.	101.5±1.4	111.7±1.7	108.2±3.

$$f(t) = A\left(\frac{m}{2\pi k}\right)^{3/2}\left(\frac{x}{t}\right)^{n} e^{-m(x/t-u)^2/2kT}\left(\frac{-xdt}{t^2}\right). \quad (4)$$

Typically, PLD of YBCO yields forward directed speeds of $u\sim 10^6$ cm/s[1,9,15,16] and speed distributions characterized by temperatures of up to $T\leqslant 35\,000$ K.[14] Results depend significantly on laser energy, laser spot size, detector location, and background gas pressure. Usually, the TOF data are limited to a few fixed locations within the plume and the evolution of the distribution as the plume propagates away from the target is not explored.

A fit of Eq. (4) to the PMT TOF data similar to that shown in Fig. 3 yields the fit parameters provided in Table II. For the broadband filter at $\lambda=550\pm5$ nm, there is some ambiguity in the application of Eq. (4), as the observed emission arises from multiple atomic species. Indeed, the interpretation of the fit parameters as a single temperature and streaming speed is flawed. In this case we use the mass of barium to report the fit parameters in Tables II and III. However, the reproducibility of the PMT and imaging sensors is well represented by the variance in the observed fit parameters. Fits for multiple values of the integer exponent, n, are provided, and discussed below. The variability in extracted streaming speeds ($\sim 8\%$) and temperatures ($\sim 20\%$) for the average signal from the three PMTs viewing the same distance from the target is considerably larger than the statistical errors of $\sim 1\%$. These systematic errors are attributed to variations in viewing volumes defined by the slit assemblies. Similar results using the CCD imagery analyzed for the same target distance as the three PMT sensors are provided in Table III. Note that streaming speeds are systemically larger (2%–15%) and the temperatures lower (6%–8%) for the imagery data compared to the PMT sensors at the slot 6 location of $x=38$ mm.

TABLE III. Comparison of speed distributions from simultaneous imagery and PMT sensors at $x=3.6$ cm from TOF profiles presented in Fig. 7.

	u (10^3 cm/s)		T (1000 K)	
n	ICCD	PMT	ICCD	PMT
0	747.8±1.9	732.1±0.7	75.1±1.2	80.3±0.5
1	679.6±3.0	657.9±1.2	81.3±1.5	87.3±0.6
2	599.4±4.8	570.1±2.1	88.5±1.8	95.3±0.8
3	504.2±7.7	465.2±3.3	97.0±2.3	105.±1.0
4	389.8±12.	337.8±5.3	107.±2.9	116.±1.3
5	250.0±18.	180.6±8.3	119.±3.8	130.±1.7
6	268.6±24.	203.1±10.	98.3±4.4	115.±1.8

The streaming speeds reported in Tables (2) and (3) based on the PMT sensors are in good agreement, particularly for the lowest integer exponents, n. However, the corresponding temperatures exhibit a greater difference. Considerably more averaging (640 pulses) was performed in the data sets corresponding to Fig. 2 and Table II. In addition, the data of Fig. 7 and Table III were recorded 6 months later. Systematic changes in target wear, laser spot size, and other uncontrolled deposition conditions lead to significant differences in plume dynamics. Indeed, temperature, or the width of the speed distribution, may be an important process control parameter.

A thorough examination of the evolution of the TOF profiles and kinetic energy distributions as the plume propagates from the target to the substrate is enabled by the imagery based TOF data. By employing the narrow band filters, the emission is limited to a single emitter and the extracted temperatures and streaming speeds reflect the kinetic energy distributions for the indicated species. The results of fitting Eq. (4) with $n=0$ and $n=-2$ to the TOF profiles for all target distances, x, for the both the Ba I and Y I filters are provided in Figs. 8 and 9. There is a systematic variation in the extracted speeds, u, and temperatures, T, depending on the exponent, n, as shown in Fig. 10.

Considerable discussion regarding the theoretically appropriate value for n is found in the literature, with $n=3$ (or $n=4$ for flux monitoring detectors) commonly used.[1,9,12–14,20,21] The modified Maxwellian distribution of Eq. (4) assumes the speed distribution has equilibrated after propagating a short distance from the ablated target, and that signal is a direct measure of the concentration of the indicated specie. Emission time-of-flight profiles monitor the concentration of excited (emitting) states. The collisional processes by which the electronically excited atoms are produced also depend on the cross sections as a function of relative kinetic energy. If the collision energy is significantly above threshold (easily satisfied in PLD) and the additional reagent channels are not accessible (poorly satisfied in PLD systems where many excited states, oxide products, etc. are accessible), then a weak dependence of excitation rate on relative speed might be expected.

While any single TOF profile is adequately represented

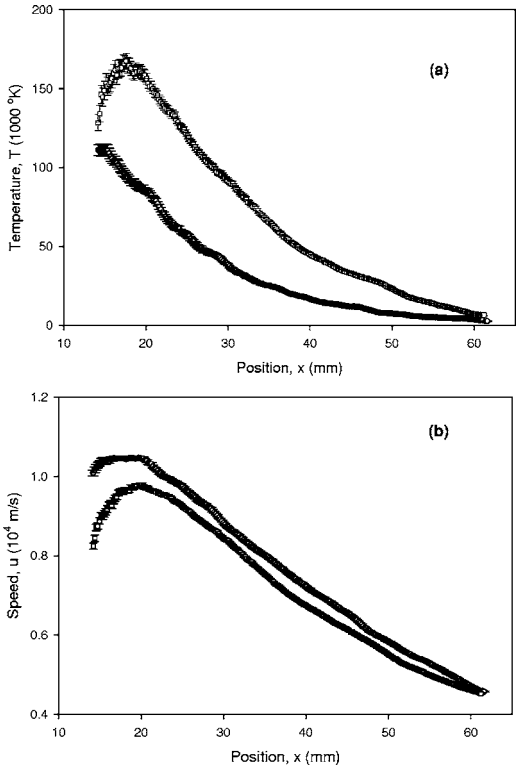

FIG. 8. (a) Temperature, T, and (b) streaming speeds, u, for $n=-2$ using the (○) Y I $\lambda=547\pm1$ nm and (□) Ba I $\lambda=767\pm1$ nm filters. Oxygen background pressure is 200 mTorr.

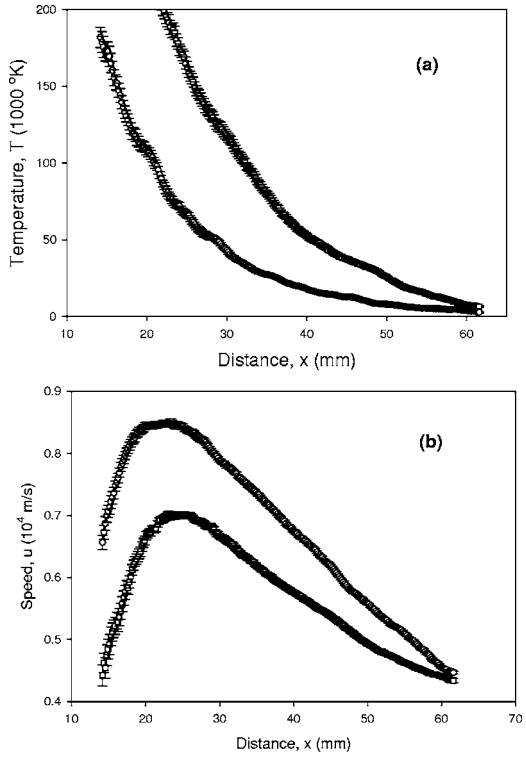

FIG. 9. (a) Temperature, T, and (b) streaming speeds, u, for $n=0$ using the (○) Y I $\lambda=547\pm1$ nm and (□) Ba I $\lambda=767\pm1$ nm filters. Oxygen background pressure is 200 mTorr.

by the modified Maxwellian distribution of Eq. (4), the quality of the fits are relatively insensitive to the exponent, n. However, there are several trends exhibited in Figs. 8–10 suggesting difficulty with a universal interpretation of an evolving Maxwellian distribution: (1) at moderate distances from the target ($x=14.7$ mm), negative streaming speeds are attained; (2) for $n\geqslant 0$, an apparent acceleration of the plume is observed for distances as great as $x=25$ mm; and (3) the best fits are achieved for $n<0$, sometimes as low as $n=-4$. The new imaging TOF instrumentation provides a full description of the evolving kinetic energy distributions, and it appears that characterizing the distributions by an evolving temperature and streaming speed is a poor representation of the plume dynamics.

Very high temperatures, $T\sim 200\,000$ K, are observed near the target, particularly for larger values of the exponent, n. Even at $x=5$ cm the temperatures are $\sim 10\,000$ K. It is important to note that these streaming temperatures represent the width of the forward directed speed distribution function. For a time-of-flight profile, $f(t)$, which propagates without change in streaming speed or temperature, the width the profile increases at larger target distances, but the ratio of the width to the most probable time is a constant. At $T=600\,000$ K ($kT\sim 52$ eV), the profile width nearly equals the peak time. Temperatures as high as $T=350\,000$ have been reported at target distances as great as 72 mm.[12]

The neutral yttrium emitters are represented by a higher streaming speed and lower temperature than neutral barium. The streaming speeds of the two species approach a common value at greater target distances, whereas Ba I retains a higher temperature (broader TOF profile) even at large target distances. The heavier barium atoms carry more momentum and thus impart less kinetic energy to the background oxygen gas per collision than the lighter yttrium. As a result, the Ba I kinetic energy distribution remains broader (higher temperature) as the plume evolves.

The imaging TOF apparatus offers an advantage in data acquisition time. For the PMT and imaging TOF spectra with signal to noise characteristics as compared in Fig. 7, the PMT spectra required 640 laser pulses to obtain a profile at a single target distance. The imaging sensor requires one laser shot to record an image at a single time delay. An entire TOF profile was developed over 140–200 laser pulses with 100–250 ns increments between snapshots. Increasing the temporal resolution to 50 ns would require 400–700 laser

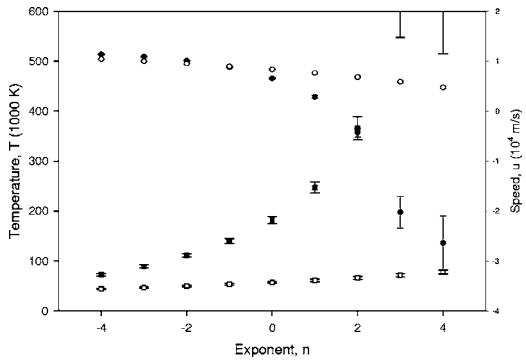

FIG. 10. The systematic variation of extracted temperatures, T, (■,□) and streaming speeds, u, (●,○) for Y I (using the $\lambda=547\pm1$ nm filter) with Eq. (4) distribution function exponent, n, for a target distance of $x=14.7$ mm (■,●) and $x=26.3$ mm (□,○).

pulses and a data acquisition time similar to the single PMT profile. The imaging sensor provides a complete spatial map of the TOF profiles in approximately the same acquisition time as the PMT provides a single profile. However, the imaging sensor currently requires postprocessing of the images, whereas the PMT yields the TOF profile directly. Furthermore, the imaging sensing trades improved spatial resolution at the expense of reduced temporal resolution. However, the PMT sensor's intrinsic temporal resolution of ~2 ns cannot be fully realized, as the plume propagates about 1 mm (minimum spatial resolution) in ~100 ns.

The use of fast imaging sensors to obtain emission time-of-flight profiles during pulsed laser deposition offers several advantages over traditional nonimaging techniques: (1) complete, simultaneous mapping of the spatial evolution of the plume speed distributions; (2) reproducible, well defined spatial resolution and field of view; (3) convenient implementation on many PLD chambers; and (4) simultaneous recording of additional plume dynamics such a angular distributions and shock dynamics. However, the production of TOF profiles from imagery may require minimal averaging to remove pulse to pulse jitter and intensities fluctuations. The resulting TOF profiles compare quit favorably with fixed sensor data. The imagery based TOF profiles exhibit less intensity in the wings of the profile than the corresponding fixed point sensors. However, systematic variations in extracted streaming speed and temperatures between imaging and nonimaging sensors is less than the variation in nonimaging sensors viewing the same plume.

[1] D. Christy and G. Hubler, *Pulsed Laser Deposition of Thin Films* (Wiley, New York, 1994).
[2] R. Singh and D. Kumar, Mater. Sci. Eng., R. **22**, 113 (1998).
[3] S. R. Foltyn, P. N. Arendt, P. C. Dowden, R. F. DePaula, J. R. Groves, J. Y. Coulter, Q. X. Jia, M. P. Maley, and D. E. Peterson, IEEE Trans. Appl. Supercond. **9**, 1519 (1999).
[4] S. R. Foltyn *et al.*, Physica C **341–348**, 2305 (2000).
[5] Y. Li, K. Zdun, J. Hope, J. Xie, S. Corcoran, Y. Qiao, J. Reeves, K. Lenseth, and V. Selvamanickam, IEEE Trans. Appl. Supercond. **13**, 2758 (2003).
[6] V. Selvamanickam, Y. Li, S. Sathiaraju, Y. Qiao, K. Zdun, L. Hope, J. Reeves, K. Lenseth, and P. Haldar, *Proceedings of the Space Technology and Applications International Forum*, STAIF 2002, Albuquerque, NM, 2002, p. 1163 (2002).
[7] R. R. Biggers *et al.*, Eng. Applic. Artif. Intell. **11**, 627 (1998).
[8] R. R. Biggers, G. Kozolowski, and J. Jones, Integr. Ferroelectr. **28**, 201 (2000).
[9] K. Fukushima, Y. Kanke, and M. Badaye, J. Appl. Phys. **77**, 5406 (1995).
[10] D. B. Geohagen, Thin Solid Films **220**, 138 (1992).
[11] D. B. Geohegan, Appl. Phys. Lett. **60**, 2732 (1992).
[12] J. P. Zheng, Z. Q. Huang, and D. T. Shaw, Appl. Phys. Lett. **54**, 280 (1989).
[13] R. Zheng, M. Campbell, K. W. D. Ledingham, W. Jia, C. T. J. Scott., and R. P. Singhal, Spectrochim. Acta, Part B **52**, 339 (1997).
[14] C. E. Otis and P. M. Goodwin, J. Appl. Phys. **73**, 1957 (1993).
[15] D. B. Geohagen and D. N. Mashburn, Appl. Phys. Lett. **55**, 2345 (1989).
[16] Y. Nakata, H. Kaibara, T. Okada, and M. Maeda, J. Appl. Phys. **80**, 2458 (1996).
[17] D. Riley, L. Doyle, and R. Al-Wazzan, J. Appl. Phys. **79**, 7223 (1996).
[18] R. Payling and P. Larkins, *Optical Emission Lines of the Elements* (Wiley, New York, 2000).
[19] S. S. Harilal, C. V. Bindhu, M. S. Tillack, F. Najmabadi, and A. C. Gaeris, J. Appl. Phys. **93**, 2380 (2003).
[20] R. Kelly and R. W. Dreyfus, Surf. Sci. **198**, 263 (1988).
[21] J. C. S. Kools, T. S. Baller, S. T. DeZwart, and J. Dieleman, J. Appl. Phys. **71**, 4547 (1992).